ACS APPLIED MATERIALS & INTERFACES

Research Article

www.acsami.org

Improved Elevated Temperature Performance of Al-Intercalated V_2O_5 Electrospun Nanofibers for Lithium-Ion Batteries

Yan L. Cheah,[†] Vanchiappan Aravindan,[‡] and Srinivasan Madhavi*[,†,‡,§]

[†]School of Materials Science and Engineering, Nanyang Technological University, Singapore 639798

[‡]Energy Research Institute (ERI@N), Nanyang Technological University, Research Techno Plaza, 50 Nanyang Drive, Singapore 637553

[§]TUM-CREATE Center for Electromobility, Nanyang Technological University, 50 Nanyang Drive, Singapore 637553

Supporting Information

ABSTRACT: Al-inserted vanadium pentoxide (V_2O_5) nanofibers (Al-VNF) are synthesized by simple electrospinning technique. Powder X-ray diffraction (XRD) patterns confirm the formation of phase-pure structure. Elemental mapping and XPS studies are used to confirm chemical insertion of Al in VNF. Surface morphological features of as-spun and sintered fibers with Al-insertion are investigated by field-emission scanning electron microscopy (FE-SEM). Electrochemical Li-insertion behavior of Al-VNFs are explored as cathode in half-cell configuration (vs. Li) using cyclic voltammetry and galvanostatic charge−discharge studies. Al-VNF ($Al_{0.5}V_2O_5$) shows an initial discharge capacity of ∼250 mA h g^{-1} and improved capacity retention of >60% after 50 cycles at 0.1 C rate, whereas native VNF showed only ∼40% capacity retention at room temperature. Enhanced high current rate and elevated temperature performance of Al-VNF ($Al_{1.0}V_2O_5$) is observed with improved capacity retention (∼70%) characteristics. Improved performance of Al-inserted VNF is mainly attributed to the retention of fibrous morphology, apart from structural stabilization during electrochemical cycling.

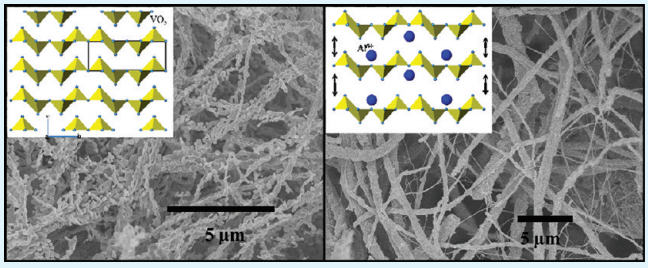

KEYWORDS: *Li-ion batteries, cathode, electrospinning, vanadium pentoxide (V_2O_5) nanofibers, rate capability, elevated temperature performance*

1. INTRODUCTION

Lithium-ion batteries (LIB) are one of the promising energy storage technologies in this era for portable applications like camcorders, laptops and electronic gadgets.[1−3] Several research works are devoted to employ such LIB power packs for zero-emission transportation applications like electric vehicle (EV) and hybrid electric vehicles (HEV).[4] Since the commercialization of LIB power packs, graphite anode has dominated the battery industry. Nevertheless, the graphitic anode serves essentially as a buffer medium for Li storage, which must be tuned to the inadequate capacity of the selected cathode material.[5] On the other hand, the commercially available cathodes like $LiCoO_2$, $LiMn_2O_4$, $LiFePO_4$, and its derivatives are capable of exhibiting practical capacity of <200 mA h g^{-1}.[6−8] Obviously, the route to any appreciable advance in Li-ion battery performance must clearly lie in the direction of improving the cathodes with higher specific capacities. Layered V_2O_5 undergoes multiple Li-insertion/extraction reactions, thus resulting in high theoretical capacity of ∼400 mA h g^{-1}. This can be attributed to its multiple oxidation states (V^{5+}, V^{4+}, and V^{3+}) and hence is a promising candidate for high capacity cathodes.

V_2O_5 offers several advantages such as low cost and abundance on earth crust.[9] At the same time, problems such as severe capacity fading and poor rate capability inhibit its practical LIB application. Poor Li-diffusion kinetics, structural instability with Li-intercalation/deintercalation and inherent electronic conductivity (∼1 × 10^{-2} to ∼1 × 10^{-3} S cm^{-1}) of V_2O_5 are main causes of the aforementioned issues.[10,11] Studies have shown that nanostructured V_2O_5 exhibits higher initial capacity as compared to bulk V_2O_5 owing to their small particle size, micro/nano structure morphology which provides shortened Li-diffusion pathways.[12−14] In addition, to overcome the said issues the morphology is fine-tuned to improve the Li^+ ion diffusion by creating more open structures and incorporation of conductive coatings[15−17] to increase the conductivity by synthesizing the V_2O_5 in one-dimensional (1D) nanostructures.[1,12−15,18−22] Inclusion of transition metal cations like Al^{3+} and Ag^+ into V_2O_5 layers leads to the formation of [MO_6] octahedral units that enhance the structural stability during Li-intercalation/deintercalation.[23]

In the present work, an attempt has been made to synthesize one-dimensional (1D) V_2O_5 nanofibers (VNF) with inclusion of various amounts of Al in the V_2O_5 interlayer ($Al_{0.5}$VNF and

Received: April 9, 2012
Accepted: May 22, 2012
Published: May 22, 2012

$Al_{1.0}$VNF) by electrospinning technique. Electrospinning is a simple, cost-effective method which enables the nanofibers with high aspect ratio and a large surface area-to-volume ratio.[1,12,13,15,21,24,25] Tunable surface morphology and diameter of the fibers is easily controlled by varying parameters such as the applied potential, viscosity and flow rate of the precursor. For LIBs applications, porous and highly interconnected nanoparticle network of nanofibers electrode provides higher electrode/electrolyte contact surface with facile diffusion pathways. Extensive characterizations were carried out for the electrospun VNF, $Al_{0.5}$VNF, and $Al_{1.0}$VNF fibers and electrochemical properties were evaluated by means of half-cell configuration with different testing conditions. The obtained results are described in detail.

2. EXPERIMENTAL SECTION

2.1. V_2O_5 Synthesis and Characterization. For the preparation of Al-VNFs, the precursors vanadyl acetylacetonate ($VO(acac)_2$, 98%, Sigma-Aldrich, 2.65 g), poly (vinylpyrrolidone) (PVP, M_w 360 000, Fluka), acetic acid (Tedia Company Inc.) and absolute ethanol (Fluka) were used as received. The synthesis procedure of VNF was slightly modified for chemical insertion of Al^{3+} ions from our previous work.[14,22,26] Acetic acid and absolute ethanol was used in 1: 9 volume ratio and 0.012 and 0.03 g mL^{-1} of aluminum nitrate ($Al(NO_3)_3$, Riedel de Haën, >98%) was added to obtain $Al_{0.5}$VNF and $Al_{1.0}$VNF phases respectively. The well-mixed precursor was electrospun using applied DC voltage of 10 kV between the needle tip and aluminum foil collector. The distance between needle and Al collector was kept a distance of 10 cm with flow rate of 1.5 mL h^{-1}. As-spun fibers were then heat-treated at 400 °C for 15 min in air with a heating and cooling rate of 2 °C min^{-1} to yield the resultant phase.

Morphological features of Al-inserted and native VNFs were studied using field emission scanning electron microscope (FE-SEM, JEOL JSM-7600F) with an accelerating voltage of 5 kV and a transmission electron microscope (TEM, JEOL 2100F) in high resolution mode operating at 200 kV attached with elemental mapping. Structural properties of Al-inserted and native VNF were examined using Bruker X-ray diffractometer using Cu−Kα radiation between 10 to 80 °. The obtained X-ray diffraction (XRD) patterns were analyzed by Rietveld refinement[27,28] using Topas V3 (Bruker-AXS) software by fundamental parameters approach.[29] X-ray photoelectron spectroscopy (XPS) was performed with an Axis Ultra (Kratos) spectrometer with monochromatic Al−Kα excitation and analyzed using CasaXPS software (Version 2.3.15).

2.2. Electrode Fabrication Process. Composite cathodes were formulated by mixing active material (V_2O_5), binder (Kynar 2801), and conductive additive (Super P Li carbon, Timcal) in the weight ratio 60:20:20, respectively, using 1-methyl-2-pyrrolidinone (NMP, Sigma-Aldrich) as solvent for binder to form slurry. The resulting viscous slurry was subsequently coated over aluminum foil using a doctor blade. Al foils were dried in a vacuum oven for several hours to remove the solvent molecules and pressed in between the twin rollers to provide necessary adherence toward Al current collector. The dried composite VNF electrodes were punched out with 16 mm diameter blanks and same area of counter electrode lithium foil (~0.59 mm thick, Hohsen Corporation, Japan) was used for the fabrication of test cells. The lithium insertion properties were evaluated in half-cell configuration using two-electrode CR 2016 coin cell assembly. The coin-cells were fabricated under Ar filled glovebox (MBraun) and the electrodes were separated by Celgard 2400 separator. The 1 M $LiPF_6$ in ethylene carbonate (EC):diethyl carbonate (DEC) (1:1 wt.%, Danvec) binary mixture was used as electrolyte solution.

Galvanostatic discharge−charge profiles of Al-inserted and native VNF based test cells were conducted between 1.75 and 4 V vs Li at ambient and elevated temperature (55 °C) conditions, using battery testing systems (Neware) at constant current mode. Cyclic voltammetric (CV) traces were recorded using Solartron 1470E potentiostat in two-electrode configuration at scan rate of 0.1 mV s^{-1}, in which metallic lithium serves as both counter and reference electrode.

3. RESULTS AND DISCUSSIONS

3.1. Morphological and Compositional Studies. Figure 1 represents the surface morphological features of as-spun and

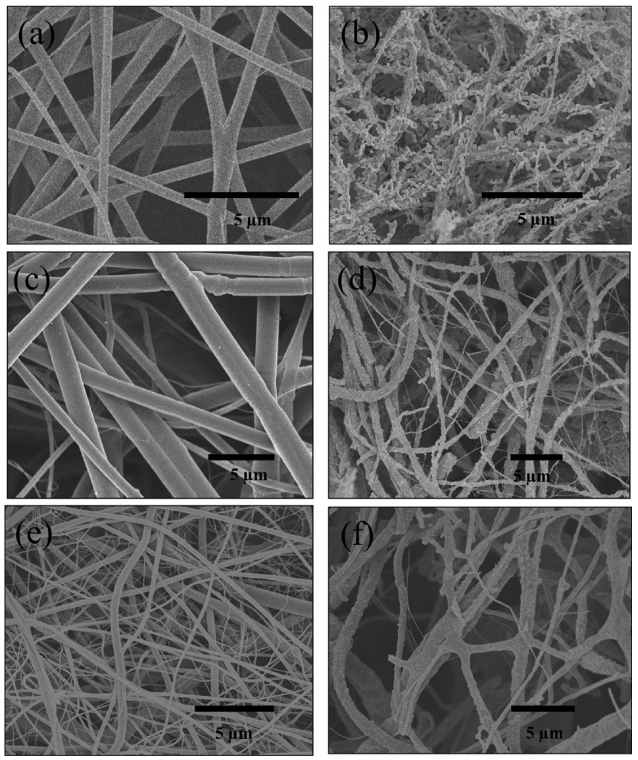

Figure 1. Field-emission secondary electron (FE-SEM) images of as-spun (a) VNF, (c) $Al_{0.5}$VNF, (e) $Al_{1.0}$VNF and sintered (b) VNF, (d) $Al_{0.5}$VNF, and (f) $Al_{1.0}$VNF, respectively.

sintered VNFs with and without Al insertion. From a, c, and e in Figure 1, the formation of smooth morphology with long aspect ratios and mainly with fiber diameters ranging from 500 to 800 nm for VNF, $Al_{0.5}$VNF, and $Al_{1.0}$VNF, respectively, is apparent. Incorporation of $Al(NO_3)_3$ in to the VNF precursor leads to a slight decrease in viscosity of the solution, which results in a lower flow rate (1.5 mL h^{-1}) during the electrospinning process compared to native VNF fibers (2 mL h^{-1}). As a result, it gives rise to larger size distribution of fibers in the Al-VNFs with reduced thickness (~100−200 nm) as can be seen from the Figures 1c and e. Sintering at 400 °C for 15 min in air results in the formation of porous fibers for pure V_2O_5 and the obtained morphology is similar to our previous work (Figure 1b).[14] Nevertheless, polycrystalline fibers are obtained in the case of Al-VNF (Figures 1d, f and 2a, b) with surface area of ~9−10 m^2 g^{-1} irrespective of the Al doping and heat treatment. Transmission electron microscopy (TEM) also revealed the presence of porous fibers, irrespective of Al insertion (Figure 2). The presence of such porous structure is expected to enable the facile insertion/extraction of Li-ions and thereby providing better electrochemical properties, especially at high current rates. Elemental analysis was carried out to estimate the amount of Al^{3+} present in the V_2O_5 layers of two samples synthesized resulted in Al:V molar ratios of 1:4 and 1:2, respectively. Hereafter, the former and latter compositions are denoted as $Al_{0.5}$VNF and $Al_{1.0}$VNF,

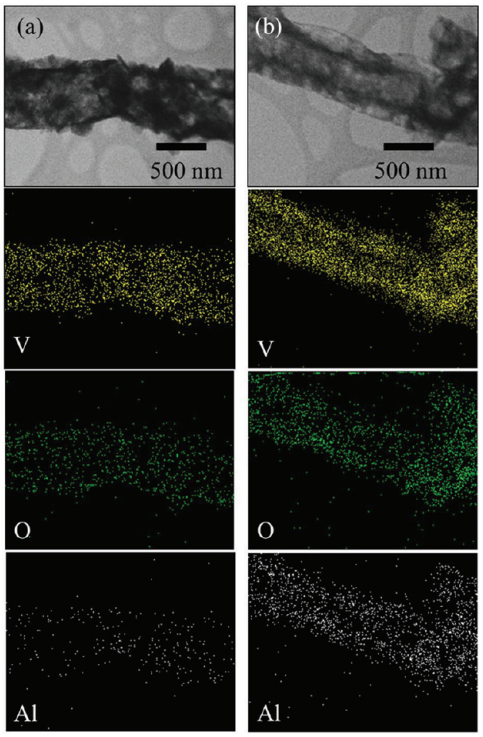

Figure 2. Transmission electron (TEM) images and corresponding Al, V ,and O (as labeled) elemental maps of (a) $Al_{0.5}VNF$ and (b) $Al_{1.0}VNF$, respectively.

respectively. Mapping is one of the efficient techniques to study the distribution of elements in the specified area. Figure 2 shows the elemental mapping of Al-VNF with two different compositions and it was recorded during TEM analysis. It is evident that, $Al_{0.5}VNF$ and $Al_{1.0}VNF$ showed the even distribution of Al^{3+} throughout the area mapped according to the concentration of the inserted element.

The XRD patterns of Al-inserted and native VNFs were collected and presented in Figure 3. Rietveld refinements were carried out for all the three samples (VNF, $Al_{0.5}VNF$ and $Al_{1.0}VNF$) using TOPAS software. The observed reflections for VNF, $Al_{0.5}VNF$ and $Al_{1.0}VNF$ clearly indicate the formation of phase pure structure without any impurity traces or preferred orientation. The crystalline peaks were indexed according to the layered Shcherbinaite structure with $Pmn2_1$ space group. The lattice parameter values of VNF are calculated by Rietveld refinement (see the Supporting Information, Figure S1) and found to be a = 11.5181(1) Å, b = 4.3805(4) Å and c = 3.5671(2) Å. Variations in the lattice parameter values are noted for inclusion of Al; $Al_{0.5}VNF$ is a = 11.5197(2) Å, b = 4.3756(9) Å and c = 3.5675(6) Å; and $Al_{1.0}VNF$ a = 11.5202(3) Å, b = 4.3783(1) Å and c = 3.5704(1) Å. The observed values are consistent with the literature values (JCPDS 89−2482 a = 11.5202(3) Å, b = 4.3783(1) Å and c = 3.5704(1) Å) Inclusion of Al in the V_2O_5 structure results in the decrease of crystallite size values and found to be 98(2), 47(1) and 33(1) nm for VNF, $Al_{0.5}VNF$ and $Al_{1.0}VNF$, respectively. This clearly indicates influence of Al^{3+} ion toward the structural properties of V_2O_5. Reduction in the crystallite size values are apparently reflected from the decrease in the intensity and broadening of the peaks evidenced from XRD patterns. From the increase in the a and c lattice parameters from the native VNF to the Al-inserted VNF, it can be deduced

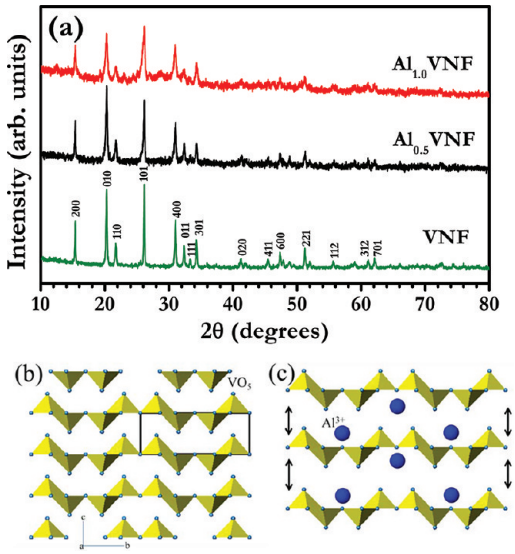

Figure 3. (a) X-ray diffraction (XRD) patterns of VNF, $Al_{0.5}VNF$, and $Al_{1.0}VNF$ and schematic representation of (b) V_2O_5 (Shcherbinaite) crystal structure and (c) V_2O_5 lattice (not to scale) with possible positions of Al atoms, as indicated by blue spheres, and possible movement of V_2O_5 layers upon intercalation of lithium ions, as indicated by arrows.

that the chemically inserted Al^{3+} ions are likely to reside between the VO_5 slabs and forming the $[AlO_6]$ octahedra with oxygen atoms in the V_2O_5 structure.[23,30] Schematic representations of the layered V_2O_5 crystal structure, formed by the VO_5 polyhedra, and the possible positions of Al^{3+} ions residing within the V_2O_5 layers, are given in Figure 3b and c, respectively. The occupancy of Al^{3+} will stabilize the VO_5 layers and thereby improving the facile insertion and extraction of Li-ions under high current operations.

X-ray photo electron spectrum (XPS) of VNF, $Al_{0.5}VNF$, and $Al_{1.0}VNF$ samples with energy level of V $2p_{3/2}$ are recorded and given in Figure 4. In the native VNF, the peak is observed at

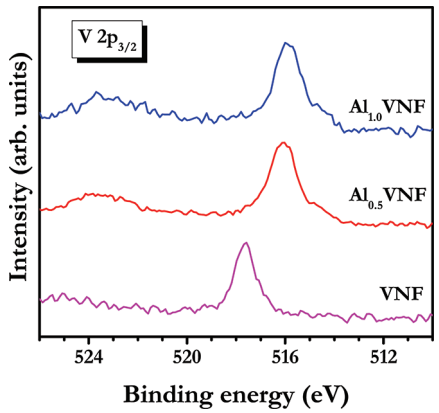

Figure 4. $V2p_{2/3}$ X-ray photoelectron spectra (XPS) of VNF, $Al_{0.5}VNF$, and $Al_{1.0}VNF$.

517.6 eV corresponds to the V^{5+} oxidation state of V_2O_5.[30,31] Introduction of Al^{3+} into the V_2O_5 lattice leads to the shifting of binding energy in to lower energy levels and evident from the energy level spectra of V $2p_{3/2}$. The binding energy 516.0−516.1 eV indicates the presence of V^{4+} ions and the observed values are similar to VO_2 phase, in which vanadium is in 4+

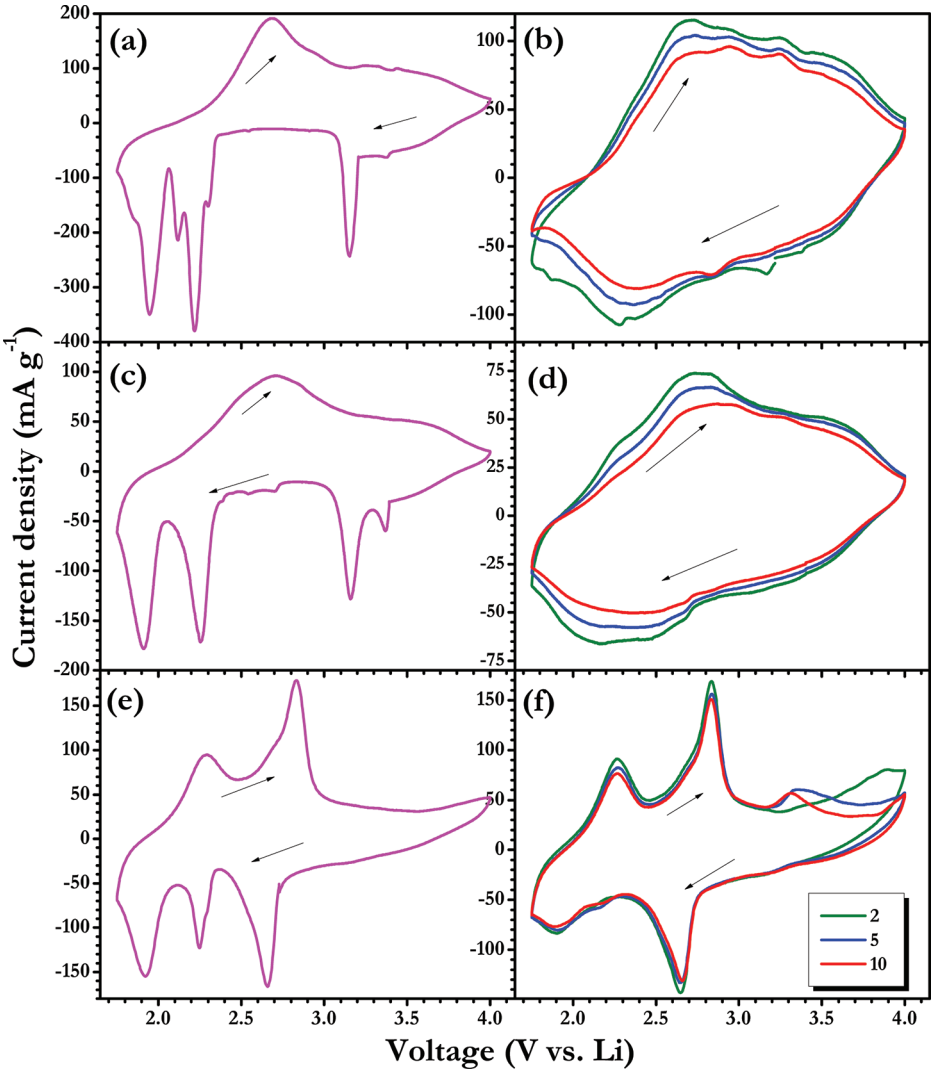

Figure 5. Cyclic voltammograms showing first cycles of (a) VNF, (c) $Al_{0.5}$VNF, and (e) $Al_{1.0}V_2O_5$ and subsequent cycles of (b) VNF, (d) $Al_{0.5}$VNF, and (f) $Al_{1.0}$VNF, respectively, in which metallic lithium serves as both counter and reference electrodes in two electrode coin cell configuration at scan rate of 0.1 mV s^{-1} between 1.75 and 4.0 V vs Li. Integer represents cycle number.

state.[30,31] In the case of $Al_{1.0}$VNF, a small shoulder at 514.0 eV is noted which indicates the presence of mixed valence state of vanadium (V^{3+} and V^{4+}).[31] $Al_{0.5}$VNF possibly contains the mixed valence states of V^{5+} and V^{4+}, which is necessary to balance the net charge in the crystal structure of V_2O_5 matrix because of the accommodation of Al^{3+} ions. At the same time, the crystal structure of V_2O_5 is still intact and evident from the XRD reflections obtained above. The molar ratio of Al:V are in good agreement with elemental analysis described above and formula for $Al_{0.5}$VNF can be written as $Al_{0.5}(V^{5+}{}_{0.5}\ V^{4+}{}_{1.5})O_5$. Similarly for $Al_{1.0}$VNF, the larger amount of Al^{3+} inserted leads to the formation of V^{4+} and V^{3+} ions in place of V^{5+}. In combination with the elemental analysis, the molecular formula is derived to be $Al_{1.0}(V^{4+}{}_{1.0}V^{3+}{}_{1.0})O_5$.

3.2. Electrochemical Studies. Electrochemical properties of the Al-inserted and native VNF were evaluated by means of both galvanostatic and potentiostatic modes in half-cell (Li/VNF) configurations. Generally, insertion of Li-ions into V_2O_5 layers results the transformation of V_2O_5 in to $Li_xV_2O_5$ phase. Thus results the distortion in layered structure due to the occupancy of Li^+ ions into the spaces between the layers of VO_5 octahedral unit. Slow scan (scan rate 0.1 mV s^{-1}) cyclic voltammograms (CV) of Li/VNF, Li/$Al_{0.5}$VNF and Li/$Al_{1.0}$VNF cells are collected in the range between 1.75 and 4.0 V vs Li to understand the phase transformation during Li-intercalation/deintercalation and presented in Figure 5. The following equation describes the overall Li-intercalation mechanism in V_2O_5 matrix,

$$V_2O_5 + xLi^+ + xe^- \leftrightarrow Li_xV_2O_5 \quad (1)$$

The test cells are first discharged to intercalate the Li-ions in to V_2O_5 lattice. In the first cycle (Figure 5a, c, e), several oxidation/reduction peaks are observed for the Al-inserted and native VNF corresponding to the intercalation/deintercalation processes of Li-ions in V_2O_5. For VNF and $Al_{0.5}$VNF, the reduction (cathodic) peaks are observed at ~3.37, ~3.16, ~2.22, and ~1.90 V vs Li. In addition, $Al_{0.5}$VNF has a smaller reduction peak at ~3.16 V vs Li when compared to native VNF, and in addition smaller peaks are also observed at ~2.71 and ~2.54 V vs Li. On the other hand, vanishing of reduction peaks at ~3.37 and ~3.16 V are noted for $Al_{1.0}$VNF phase when compared to native VNF and $Al_{0.5}$VNF phases. Appearance of remaining reduction peaks are noted at ~2.66, ~2.22, and ~1.9 V vs Li in both cases. For VNF and $Al_{0.5}$VNF, showed a broad

oxidation (anodic) peak at ~2.70 V vs Li and showing variation in area under the curve, whereas two sharp oxidation peaks are observed for $Al_{1.0}$VNF at ~2.28 and ~2.83 V vs Li. Current densities of the Al-inserted Al-VNFs also appear to be less than that of native VNF, which could be attributed to the presence of Al^{3+} ions occupied between the layers. Wei et al.[32,33] also noted the similar kind of reduction in current densities while introducing metal-ion on V_2O_5 lattice. The appearances of cathodic peaks are indicative of the multistep reduction of V^{5+} in V_2O_5 within the voltage range 1.75 to 4.0 V vs Li[14]. The cathodic peaks at ~3.37 and ~3.16 V vs Li indicates the reduction of V^{5+} to V^{4+}, leads to the formation of ε-$Li_xV_2O_5$ phase, which is observed only for VNF and $Al_{0.5}$VNF phases. The absence of V^{5+} in $Al_{1.0}$VNF is well reflected in CV measurements and it is in good agreement with XPS data. The other cathodic peaks ~2.22 and ~1.90 V vs Li belongs to partial reduction of V^{4+} to V^{3+} and this reduction reveal the formation of δ- and γ-$Li_xV_2O_5$ mixed phases. Presence of additional reduction peak at ~2.71 V vs Li for $Al_{0.5}$VNF and ~2.66 V vs Li for $Al_{1.0}$VNF could be attributed to the increased instances of reduction of V^{4+}. Cycling below 2.0 V vs Li leads to the formation of irreversible γ-$Li_xV_2O_5$ phase which is confirmed by the appearance of reduction peak at ~1.90 V vs Li and it is noted for all three VNFs tested.[34]

Subsequent electrochemical cycling in potentiostatic modes are given in Figure 5b, d, and f. The observed traces in the successive cycles are entirely different from the first cycle for the case of native VNF and $Al_{0.5}$VNF phases. In VNF, the reduction peak is shifted from ~2.28 to ~2.31 V vs Li for consecutive cycles, whereas oxidation peak remains at ~2.68 V vs Li. On the other hand, in $Al_{0.5}$VNF the oxidation and reduction peaks remains at same potentials. Contrary to above, $Al_{1.0}$VNF displayed the reduction and two oxidation peaks at ~2.65 and ~2.27 & ~2.84 V vs Li, respectively. The observed redox potentials are same as that of in the first cycle with intense peaks, which is due to the influence of Al^{3+} insertion. It is evident that, presence of Al^{3+} ions between the layers effectively improves the structural properties during electrochemical Li-insertion/extraction and retains the crystal structure of V_2O_5. However, in all three samples there is no deviation of shape noted from second cycle onward, which indicates the excellent reversibility of the V_2O_5 fibers during lithium intercalation and deintercalation. Further, it is obvious to notice that for VNF and $Al_{0.5}$VNF, the net area under the curve tends to decrease, which is indicative of capacity fade during cycling. Nevertheless, very small amount of reduction in the net charge under the curve is noted for $Al_{1.0}$VNF. Hence, an improved cycleability is expected for the $Al_{1.0}$VNF irrespective of the capacity.

Galvanostatic cycling profiles of Li/VNF, $Al_{0.5}$VNF and $Al_{1.0}$VNF coin cells cycled between 1.75–4.0 V vs Li at 0.1 C rate (1 C is assumed to be 350 mA h g^{-1}) in room temperature is shown in Figure 6. As expected, all the three samples showed multiple plateaus during first discharge, which is consistent with the CV analysis and representative phase transitions occurring during Li-intercalation/deintercalation.[1,13,17,35] The first discharge plateau at ~3.18 V vs. Li which is attributed to the reduction of V^{5+} to V^{4+} to enable the intercalation of Li-ions in to layered V_2O_5.[12,16,36] It is interesting to notice the vanishing of obvious plateau at ~3.18 V vs Li upon introduction of Al^{3+} ions in to the V_2O_5 matrix. For $Al_{0.5}$VNF, it is observed that the plateau at ~3.18 V vs Li is shortened when compared to native VNF which is attributed to the reduction of remaining V^{5+} in to

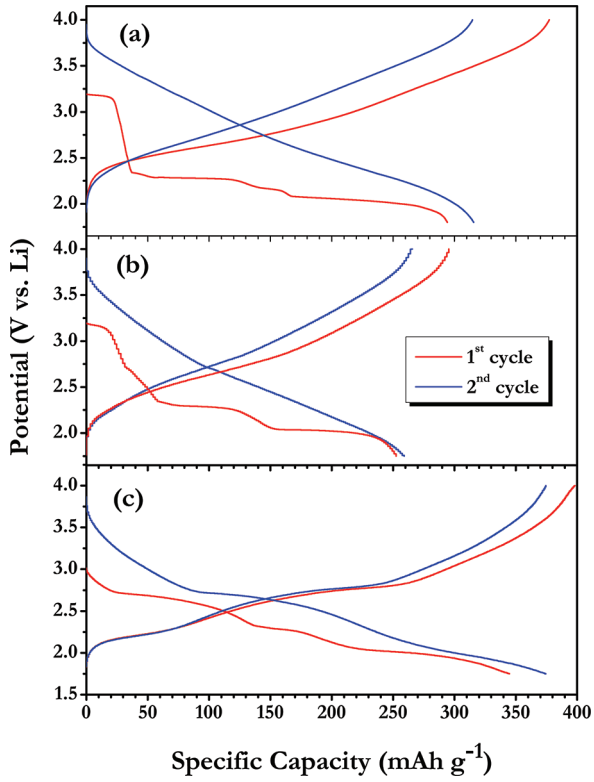

Figure 6. Typical galvanostatic traces of first two charge–discharge curves of (a) VNF, (b) $Al_{0.5}$VNF, and (c) $Al_{1.0}$VNF cells between 1.75 and 4.0 V vs Li at 0.1 C rate in room temperature.

V^{4+}. There is no such obvious plateau is observed for the $Al_{1.0}$VNF due to the unavailability of V^{5+} ions. Upon further reduction, two prominent plateaus at ~2.28 and ~2.08 V vs Li are observed for all the three cases with small shift in the range. The plateau at ~2.24 V is an indication of the formation of δ-$Li_xV_2O_5$ phase and V^{4+} is partially reduced to V^{3+} forming δ- and γ-$Li_xV_2O_5$ mixed phases. The plateau ~2.08 V vs Li is believed to be the transformation of δ-$Li_xV_2O_5$ to γ-$Li_xV_2O_5$ phase. Further discharge into 1.75 V vs Li causes the irreversible formation of γ-$Li_xV_2O_5$ phase, and this is in good agreement with CV traces obtained above. Further, the plateau ~2.3 V is also shortened and this leads to the lower initial discharge capacity of ~250 mA h g^{-1} (~1.7 mols of lithium). However, in $Al_{1.0}$VNF phase distinct plateau at ~3.12 V vs Li is not observed. Instead, observation of a broad plateau at ~2.67 V and a shortened plateau at ~2.3 V vs Li indicates the reduction of V^{4+} to V^{3+}, consistent with the CV data obtained above. The plateau observed at ~2.0 V vs Li in $Al_{1.0}$VNF is also not as sharp as observed in the case of VNF and $Al_{0.5}$VNF. In the second charge–discharge cycle, there are no plateaus observed for VNF and $Al_{0.5}$VNF, whereas shortened plateaus are observed ~2.7 V and ~2.76 V vs Li in the discharge and charge curves respectively for $Al_{1.0}$VNF, corresponding to the improved structural stability of $Al_{1.0}$VNF phase rendered by Al^{3+} insertion. This is an indication that an irreversible phase transformation of V_2O_5 to $Li_xV_2O_5$ occurred during the first discharge for VNF and $Al_{0.5}$VNF, but there is some reversibility of the phase transformation occurring in the more heavily inserted $Al_{1.0}$VNF phase which is in good agreement with the observations in CV trace. In all three samples, first charge capacity is slightly higher than discharge capacity and the observed excess capacity is obtained from the interfacial storage

across the electrolyte/electrode interface. Except for the initial cycle, all the three materials exhibited columbic efficiency over 99% in subsequent cycles, which indicates excellent reversibility during galvanostatic cycling.

As mentioned earlier, all VNF cells were cycled galvanostatically between 1.75 to 4.0 V vs Li at 0.1 C rate (35 mA g^{-1}) at room temperature and presented in Figure 7a. VNF delivered

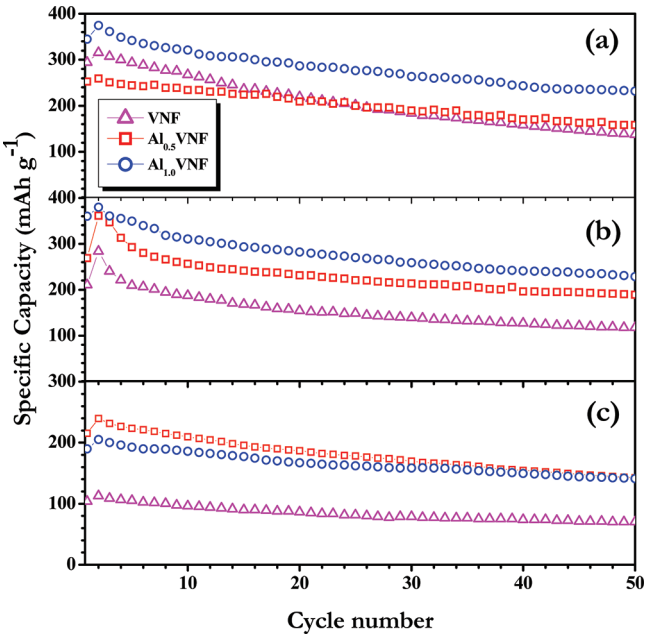

Figure 7. Plots of specific discharge capacity vs cycle number of VNF, $Al_{0.5}$VNF, and $Al_{1.0}$VNF cycled at (a) 0.1 *C* rate at room temperature and (b) 0.1 *C* rate at 55 °C and (c) 1 *C* rate at room temperature.

an initial discharge capacity of 316 mA h g^{-1} (~2.2 mols of lithium) and retained only 43% of initial capacity upon cycling to 50 cycles. $Al_{0.5}$VNF starts off with initial capacity of ~250 mA h g^{-1}, which is equivalent to ~1.7 mols of lithium and retains 63% of initial capacity after 50 cycles. The lower initial capacity could be due to the reduced transformation of V^{5+} to V^{4+}. As for $Al_{1.0}$VNF, it also displayed higher initial discharge capacity of ~350 mAh g^{-1} and maintained ~85% of cyclic retention within 20 cycles. The higher initial capacity is possibly due to the increased space between the VO_5 layers (Figure 3c), enabling initial intercalation of larger amount of Li^+ ions and conductivity as well (see the Supporting Information, Figure S2).

To study the influence of Al^{3+} insertion toward the electrochemical properties of VNF at elevated temperature conditions (55 °C) with the same current rate (0.1 *C*), galvanostatic charge−discharge studies were conducted and corresponding cycling profiles are illustrated in Figure 7b. The native VNF fibers delivered the discharge capacity of ~285 (~2 mols lithium) and ~120 mAh g^{-1} (~0.8 mols lithium) for second and 50th cycle, respectively, with ~40% capacity retention. Incorporation of Al^{3+}, $Al_{0.5}$VNF showed the initial discharge capacity of ~360 mA h g^{-1} (~2.4 mols lithium) with improved capacity retention of over 50% after 50 cycles. For $Al_{1.0}$VNF, the insertion of Al^{3+} is beneficial for achieving highest discharge capacity of ~350 mA h g^{-1} (~2.4 mols lithium) with capacity retention of ~66% after 50 cycles. It is interesting to note that the $Al_{1.0}$VNF has the highest initial capacity at 0.1 C rate for both room temperature as well as elevated temperature (55 °C) cycling. Also, the obtained result clearly shows the influence of Al^{3+} ions toward thermal stability of V_2O_5 at elevated temperature conditions. Unfortunately, there are no reports available on the high-temperature performance of V_2O_5 to compare the obtained results.

High-rate performance is one of the prerequisite for cathode materials and in order to establish the effect of Al^{3+} insertion, the test cells were cycled at 1 *C* (350 mA g^{-1}) in room temperature conditions and corresponding cycling profiles are given in Figure 7c. The cell comprising VNF showed the lower initial discharge capacity of ~114 mA h g^{-1} (~0.8 mol of lithium) when compared to ~320 mA h g^{-1} at a 0.1 *C* rate. However, the capacity retention is improved to 60% after 50 cycles. The $Al_{0.5}$VNF cell exhibited the capacity of 240 mA h g^{-1}, which is almost the same capacity at low current rates (~250 mA h g^{-1}); however, improvement in the capacity retention is noted after 50 cycles (~60%). As for $Al_{1.0}$VNF, the larger amount of Al-inclusion led to the slightly less initial capacity of ~208 mA h g^{-1} when compared to low rates (~250 mA h g^{-1} at 0.1 C rate), but enhanced capacity retention of ~70% is noted after 50 cycles. Zhan et al.[30,37] reported the synthesis of Al-inserted V_2O_5 nanopowder ($Al_{0.2}V_2O_5$) and delivered the initial discharge capacity of ~190 mA h g^{-1} at ~0.1 *C* rate with ~76% capacity retention after 50 cycles. When increasing the current rate to 0.2 C, the cell displayed a discharge capacity of ~140 mA h g^{-1} with cyclic retention of ~57% after 50 cycles. In the present work, increasing the concentration of Al^{3+} ions in the VNF matrix contributed to higher cycling stability and capacity retention at higher *C* rates. Furthermore, the porous morphology of the fibers contributed the advantage of higher initial capacity and improved capacity retention when compared to Al-inserted nanopowders.

Post-mortem analysis was carried out after electrochemical cycling to ensure the retention of fibrous morphology after the cycling. Hence, the cycled test cells were opened in an argon-filled glovebox and electrodes were carefully taken and washed with DEC and subsequently dried. For comparison, fresh test electrodes are also subjected for the FE-SEM investigations and obtained images are presented in Figure 8. From Figure 8a, it can be seen that the as-prepared VNF electrode shows the presence of nanofiber (indicated by arrow) morphology before cycling and no fibrous morphology is retained after cycling (Figure 8b). Nanofibrous morphology is observed in as-prepared electrodes of Al-VNF (arrowed, Figure 8c,e). In contrast to native VNF, the fibers are still intact (arrowed, Figure 8d,f) after the electrochemical cycling. The improved tenacity of the Al-VNF could contribute to the improved electrochemical properties, especially capacity retention during high rate testing, when compared to native VNF.

In general, Al-insertion to VNF is observed to improve the high-rate and high temperature cycling properties to a certain extent. First, the addition of Al^{3+} ions into the V_2O_5 structure leads to the reduction of V^{5+} to V^{4+} (for both $Al_{0.5}$VNF and $Al_{1.0}$VNF) and also to V^{3+} (for $Al_{1.0}$VNF) during the in situ synthesis of Al-VNFs. The presence of these prereduced vanadium ions (V^{4+} and V^{3+}) before the electrochemical Li-intercalation/deintercalation reduces the extent of electrochemically induced phase changes, related to the conversion of V_2O_5 to γ-$Li_xV_2O_5$ phase. Further, Al^{3+} insertion leads to increased *c*-spacing in the layered structure and it is believed to occupy between the VO_5 layers, thus provides the necessary structural stability for V_2O_5 phase. Once the crystal structure is stabilized and less susceptible distortion due to the

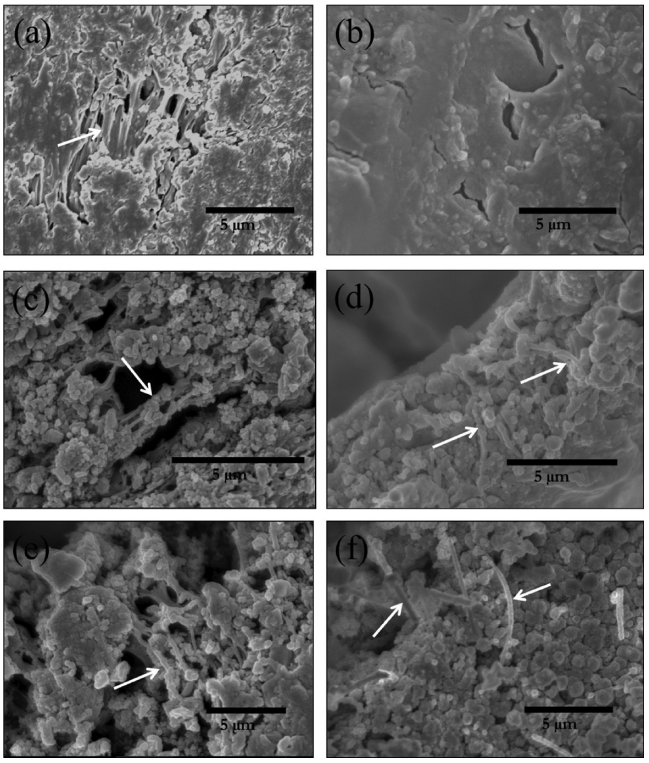

Figure 8. Field-emission secondary electron (FE-SEM) images of as-prepared electrodes of (a) VNF, (c) $Al_{0.5}$VNF, (e) $Al_{1.0}$VNF and electrochemically cycled electrodes of (b) VNF, (d) $Al_{0.5}$VNF, and (f) $Al_{1.0}$VNF, respectively.

intercalation/deintercalation of Li-ions during electrochemical cycling.[23,30] In comparison, $Al_{0.5}$VNF has more similar phase transitions during Li-intercalation/deintercalation with native VNF due to the smaller increase in the lattice parameters and presence of V^{5+} ions remains within the structure. On the other hand, $Al_{1.0}$VNF has a much larger deviation in *a* and *c* lattice parameters, and also the complete reduction of V^{5+} ions to a mixed valence states of V^{4+} and V^{3+} ions which leads to the larger differences in phase transitions related to Li-intercalation/deintercalation during electrochemical cycling. From the galvanostatic studies, it is evident that, irrespective of the inclusion of Al^{3+} at low and high current rates and testing temperature, the layered V_2O_5 showed capacity fading during cycling. There are several reasons believed for such fading, which includes vanadium dissolution,[38] poor compatibility of vanadium toward linear carbonates (DEC)[39,40] and also intrinsic nature of the native compound.[10] Further, the presence of Al^{3+} drastically improved the electrochemical performance of V_2O_5 by stabilizing the structure during high current rate and elevated temperature operations. Similar kind of improvement in the elevated temperature performance for Al^{3+} inclusion has also been noticed in other systems like $LiMn_2O_4$[41] and $Li_3V_2(PO_4)_3$.[42] At the same time, one-dimensional fibrous morphology of V_2O_5 nanofibers cannot be ruled out, which enables facile insertion/extraction of Li-ions during high current testing. The presences of voids in the fibers enable more contact area toward electrolyte solution leads to the faster diffusion of Li-ions. In addition, the retention of fibrous morphology during electrochemical testing is also one of the factors for such performance as shown by post-mortem electrode analysis.

4. CONCLUSION

Al-inserted electrospun VNF were synthesized via in situ addition of Al^{3+} ions and compared with native VNF. Formation of high aspect ratio nanofibers with diameters in the range of 500−800 nm were observed in FE-SEM. The XRD patterns reveal the formation of polycrystalline single phase V_2O_5 in Al-VNF and the inserted Al^{3+} ions occupies between the VO_5 layers of the V_2O_5 structure. The XPS studies confirm the formation of $Al_{0.5}V_2O_5$ and $Al_{1.0}V_2O_5$ phases through the valence state of vanadium. Electrochemical studies conducted in half-cell configurations reveal phase transformations in Al-VNFs, as compared to native VNF during both galvanostatic and potentiostatic measurements. The $Al_{1.0}$VNF showed enhanced high rate and elevated temperature performance due to the retention of fibrous morphology and inclusion of Al^{3+} in its crystal structure.

■ ASSOCIATED CONTENT

Ⓢ Supporting Information

Rietveld refinement and electrochemical impedance spectroscopic studies were conducted for electrospun Al-intercalated V_2O_5 nanofibers. This material is available free of charge via the Internet at http://pubs.acs.org.

■ AUTHOR INFORMATION

Corresponding Author

*E-mail: Madhavi@ntu.edu.sg. Tel.: +65 6790 4606. Fax: +65 6790 9081.

Notes

The authors declare no competing financial interest.

■ ACKNOWLEDGMENTS

This work was supported by funding from the National Research Foundation, Clean Energy Research Project grant number NRF2009EWT-CERP001-036. The authors also acknowledge Timcal for gratis providing Super P Li Carbon black. Y.L.C acknowledges the help provided by Miss Chow Shiau Kee in XPS measurements.

■ REFERENCES

(1) Scrosati, B.; Garche, J. *J. Power Sources* **2010**, *195* (9), 2419−2430.
(2) Goodenough, J. B.; Kim, Y. *Chem. Mater.* **2009**, *22* (3), 587−603.
(3) Fletcher, S. *Bottled Lightning: Superbatteries, Electric Cars, and the New Lithium Economy*; Hill and Wang: New York, 2011.
(4) Park, O. K.; Cho, Y.; Lee, S.; Yoo, H.-C.; Song, H.-K.; Cho, J. *Energy Environ. Sci.* **2011**, *4* (5), 1621−1633.
(5) Nishi, Y. *Chem. Rec.* **2001**, *1* (5), 406−413.
(6) Fergus, J. W. *J. Power Sources* **2010**, *195* (4), 939−954.
(7) Lee, K. T.; Cho, J. *Nano Today* **2011**, *6* (1), 28−41.
(8) Song, M.-K.; Park, S.; Alamgir, F. M.; Cho, J.; Liu, M. *Mater. Sci. Eng., R* **2011**, *72* (11), 203−252.
(9) Mai, L.; Xu, X.; Xu, L.; Han, C.; Luo, Y. *J. Mater. Res.* **2011**, *14*, 2175−2185.
(10) Chernova, N. A.; Roppolo, M.; Dillon, A. C.; Whittingham, M. S. *J. Mater. Chem.* **2009**, *19* (17), 2526−2552.
(11) Whittingham, M. S. *Dalton Trans.* **2008**, *40*, 5424−5431.
(12) Glushenkov, A.; Hassan, M.; Stukachev, V.; Guo, Z.; Liu, H.; Kuvshinov, G.; Chen, Y. *J. Solid State Electrochem.* **2010**, *14* (10), 1841−1846.
(13) Mai, L.; Xu, L.; Han, C.; Xu, X.; Luo, Y.; Zhao, S.; Zhao, Y. *Nano Lett.* **2010**, *10* (11), 4750−4755.
(14) Cheah, Y. L.; Gupta, N.; Pramana, S. S.; Aravindan, V.; Wee, G.; Srinivasan, M. *J. Power Sources* **2011**, *196* (15), 6465−6472.

(15) Ponzio, E. A.; Benedetti, T. M.; Torresi, R. M. *Electrochim. Acta* **2007**, *52* (13), 4419−4427.
(16) Subba Reddy, C. V.; Jin, A.-P.; Han, X.; Zhu, Q.-Y.; Mai, L.-Q.; Chen, W. *Electrochem. Commun.* **2006**, *8* (2), 279−283.
(17) Reddy, C. V. S.; Wei, J.; Quan-Yao, Z.; Zhi-Rong, D.; Wen, C.; Mho, S.-i.; Kalluru, R. R. *J. Power Sources* **2007**, *166* (1), 244−249.
(18) Ban, C.; Chernova, N. A.; Whittingham, M. S. *Electrochem. Commun.* **2009**, *11* (3), 522−525.
(19) Ragupathy, P.; Shivakumara, S.; Vasan, H. N.; Munichandraiah, N. *J. Phys. Chem. C* **2008**, *112* (42), 16700−16707.
(20) Ren, X.; Jiang, Y.; Zhang, P.; Liu, J.; Zhang, Q. *J. Sol−Gel Sci. Technol.* **2009**, *51* (2), 133−138.
(21) Tarascon, J.-M. *Philos. Trans. R. Soc., A* **2010**, *368* (1923), 3227−3241.
(22) Wee, G.; Soh, H. Z.; Cheah, Y. L.; Mhaisalkar, S. G.; Srinivasan, M. *J. Mater. Chem.* **2010**, *20* (32), 6720−6725.
(23) Giorgetti, M.; Berrettoni, M.; Smyrl, W. H. *Chem. Mater.* **2007**, *19* (24), 5991−6000.
(24) Cavaliere, S.; Subianto, S.; Savych, I.; Jones, D. J.; Roziere, J. *Energy Environ. Sci.* **2011**, *4* (12), 4761−4785.
(25) Dong, Z.; Kennedy, S. J.; Wu, Y. *J. Power Sources* **2011**, *196* (11), 4886−4904.
(26) Aravindan, V.; Cheah, Y. L.; Mak, W. F.; Wee, G.; Chowdari, B. V. R.; Madhavi, S. *ChemPlusChem* **2012**, DOI: 10.1002/cplu.201200023.
(27) Rietveld, H. *Acta Crystallogr.* **1967**, *22* (1), 151−152.
(28) Rietveld, H. *J. Appl. Crystallogr.* **1969**, *2* (2), 65−71.
(29) Cheary, R. W.; Coelho, A. *J. Appl. Crystallogr.* **1992**, *25* (2), 109−121.
(30) Zhan, S.; Wei, Y.; Bie, X.; Wang, C.; Du, F.; Chen, G.; Hu, F. *J. Alloys Compd.* **2010**, *502* (1), 92−96.
(31) Wagner, C. D.; Naumkin, A. V.; Kraut-Vass, A.; Allison, J. W.; Powell, C. J.; John R. Rumble, J. *NIST X-ray Photoelectron Spectroscopy Database Database 20*, version 3.5; National Institute of Standards and Technology: Gaithersburg, MD, 2003.
(32) Wei, Y.; Ryu, C.-W.; Kim, K.-B. *J. Alloys Compd.* **2008**, *459* (1−2), L13−L17.
(33) Wei, Y.; Ryu, C.-W.; Kim, K.-B. *J. Power Sources* **2007**, *165* (1), 386−392.
(34) Cheah, Y. L.; Aravindan, V.; Madhavi, S. *J. Electrochem. Soc.* **2012**, *159* (3), A273−A280.
(35) Sakunthala, A.; Reddy, M. V.; Selvasekarapandian, S.; Chowdari, B. V. R.; Selvin, P. C. *Energy Environ. Sci.* **2011**, *4* (5), 1712−1725.
(36) Cocciantelli, J. M.; Doumerc, J. P.; Pouchard, M.; Broussely, M.; Labat, J. *J. Power Sources* **1991**, *34* (2), 103−111.
(37) Zhan, S.; Wang, C.; Chen, G.; Du, F.; Wei, Y. *Ionics* **2010**, *16* (3), 209−213.
(38) Patoux, S.; Wurm, C.; Morcrette, M.; Rousse, G.; Masquelier, C. *J. Power Sources* **2003**, *119−121* (0), 278−284.
(39) Armstrong, G.; Canales, J.; Armstrong, A. R.; Bruce, P. G. *J. Power Sources* **2008**, *178* (2), 723−728.
(40) Tanguy, F.; Gaubicher, J.; Soudan, P.; Bourgeon-Martin, N.; Mauchamp, V.; Guyomard, D. *Electrochem. Solid-State Lett.* **2007**, *10* (8), A184−A188.
(41) Kakuda, T.; Uematsu, K.; Toda, K.; Sato, M. *J. Power Sources* **2007**, *167* (2), 499−503.
(42) Cho, A. R.; Son, J. N.; Aravindan, V.; Kim, H.; Kang, K. S.; Yoon, W. S.; Kim, W. S.; Lee, Y. S. *J. Mater. Chem.* **2012**, *22* (14), 6556−6560.